RSC Advances

PAPER

View Article Online
View Journal | View Issue

Cite this: *RSC Adv.*, 2025, **15**, 42843

Sustainable and efficient persulfate activation by pristine pumpkin seed pomace biochar: a low-energy regeneration strategy and singlet oxygen-dominated pathways

Safin A. Abdalla, [ac] Fryad S. Mustafa, [*b] Kosar Hikmat Hama Aziz, [*b] Sewara J. Mohammed [b] and Dana A. Kader [ad]

Water contamination by persistent organic pollutants like Rhodamine B (RhB) necessitates sustainable and efficient remediation strategies. This study explores the potential of pristine biochar derived from waste pumpkin seed pomace, pyrolyzed at 600 °C (PS600) and 800 °C (PS800), as a catalyst for peroxydisulfate (PDS) activation to degrade and mineralize RhB in aqueous solution. PS800 exhibited superior catalytic performance, achieving over 99.38% RhB degradation under the optimum conditions of 20 mg L^{-1} RhB, 2 g L^{-1} catalyst, pH 5.18, and 10 mM PDS within 30 minutes, with a pseudo-first-order rate constant of 0.1644 min^{-1} and significant mineralization (81.4% TOC removal in 60 min). Characterization (SEM, EDS, XRD, FTIR, XPS, N_2 sorption) revealed that PS800 possessed a relatively developed porous structure, graphitic carbon, and abundant surface functional groups (C–OH, pyridinic N) crucial for PDS activation. Remarkably, the catalyst demonstrated excellent reusability over five cycles with a simple and effective grinding regeneration method, restoring its activity. Quenching experiments identified singlet oxygen ($^1O_2$) and superoxide ($O_2^{-\bullet}$) as the dominant reactive oxygen species, with minor contributions of sulfate ($SO_4^{-\bullet}$) and hydroxyl ($^\bullet OH$) radicals. The PS800/PDS system showed robustness across a wide pH range (3–11) and in the presence of common water matrix components, except for carbonate. This work highlights PS800 as a cost-effective, environmentally friendly, simple, and low-energy regeneration method and highly efficient catalyst for advanced oxidation processes in water treatment.

Received 5th July 2025
Accepted 27th October 2025

DOI: 10.1039/d5ra04794c

rsc.li/rsc-advances

1. Introduction

The discharge of organic pollutants is a significant source of pollution, largely due to the rise in industrial activities and urbanization worldwide.[1] Synthetic organic dyes are notable pollutants among these effluents due to their persistence and potential impact on ecology and health.[2] Specifically, the textile industry contributes significantly to the problem, with estimations indicating that roughly 15% of global dye production, equivalent to 700 000 tons annually, is released as textile effluents during dyeing processes.[3] These effluents introduce complex chemical mixtures to the aquatic environment, posing dangers to human health and aquatic ecosystems. Rhodamine B (RhB), a xanthene dye used in textiles for cotton and leather dyeing, is a versatile colorant employed across the paper, plastic, and cosmetics industries.[4,5] Its pervasive use leads to its common detection in wastewater streams, indicating its status as an environmental contaminant.[2] Its chemical stability and high water solubility cause persistence in aquatic environments.[6] The stability of RhB causes frequent use in the textile industry, highlighting the necessity of effective remediation strategies.

Conventional methods for the remediation of dye-contaminated wastewater, encompassing physical, biological, and chemical treatments, are often inadequate due to limitations such as low efficiency, high energy demand, and incomplete degradation, especially for persistent organic pollutants.[7,8] While physical techniques such as membrane separation, activated carbon adsorption, and coagulation are employed, they often transfer the pollutant to another phase rather than destroying it.[9] Biological processes can be slow and ineffective for recalcitrant compounds, and chemical methods may introduce secondary pollutants.[10,11] The shortcomings of these

[a]*Department of Chemistry, College of Education, University of Sulaimani, Sulaymaniyah 46001, Kurdistan Region, Iraq*

[b]*Department of Chemistry, College of Science, University of Sulaimani, Qlyasan Street, Sulaymaniyah 46001, Kurdistan Region, Iraq. E-mail: fryad.mustafa@univsul.edu.iq; kosar.hamaaziz@univsul.edu.iq*

[c]*Department of Pharmacy, Bright Technical and Vocational Institute Pharmacy, Sulaymaniyah 46001, Kurdistan Region, Iraq*

[d]*Pharmacy Department, Komar University of Science and Technology, Sulaymaniyah 46002, Kurdistan Region, Iraq*

traditional approaches necessitate the exploration of innovative and efficient treatment technologies for the complete removal of stable and soluble dyes.

Advanced Oxidation Processes (AOPs) are a key approach in wastewater treatment, widely used for the degradation of persistent and toxic organic pollutants.[12,13] AOPs, including photocatalysis, persulfate activation, Fenton oxidation, and ozonation, generate highly reactive hydroxyl ($^{\bullet}OH$) and sulfate ($SO_4^{-\bullet}$) radicals, powerful oxidants that break down complex organic molecules into less harmful products, ideally mineralizing them into water, carbon dioxide, and inorganic ions.[14,15] Sulfate radical-based advanced oxidation processes (SR-AOPs) are effective for breaking down persistent organic pollutants because they are functional, practical, and consistent.[16] SR-AOPs offer several benefits over the Fenton process, including effectiveness across a wider pH range and a higher redox potential ($E^0(SO_4^{-\bullet}/SO_4^{2-}) = 2.6–3.1$ V compared to $E^0(^{\bullet}OH/OH^-) = 1.90–2.70$ V). SR-AOPs also have a longer lifespan (30–40 μs), produce more radicals, are easily activated by various methods, and use persulfate salts that are stable and readily available, lowering transportation and storage costs.[17,18] These features highlight the significant potential of SR-AOPs for broad use in water treatment, attracting considerable research interest.[16] The mechanism of SR-AOPs centers on the activation of persulfate ions, which can be either peroxymonosulfate (PMS, HSO_5^-) or peroxydisulfate (PDS, $S_2O_8^{2-}$). This activation generates highly reactive sulfate radicals ($SO_4^{-\bullet}$) and hydroxyl radicals ($^{\bullet}OH$). Persulfate activation can occur through both radical and non-radical pathways. In radical pathways, the O–O bond in persulfate undergoes homolytic cleavage through energy input such as light, heat, and sound (eqn (1)) or heterolytic cleavage through electron transfer (eqn (2)), producing sulfate radicals.[18] These radicals can then react further to generate other reactive species, such as hydroxyl radicals and superoxide anion radicals. In contrast, non-radical pathways, including the formation of singlet oxygen ($^1O_2$), also play a role in pollutant degradation and often show higher selectivity for specific organic compounds.[19]

$$S_2O_8^{2-} + \text{source of energy } (h\nu) \rightarrow 2SO_4^{-\bullet} \quad (1)$$

$$S_2O_8^{2-} + \text{source of electron } (e^-) \rightarrow SO_4^{-\bullet} + SO_4^{2-} \quad (2)$$

Various methods can be employed to achieve this activation, including the use of heat, ultraviolet (UV) light, alkaline environments, electrical currents, ultrasonic waves, or catalysts such as transition metals and carbon-based materials[14] Although these methods for activating persulfate are efficient, they come with notable drawbacks, including high energy requirements, high costs, and the risk of metal leaching.[20,21] To address these issues, researchers have increasingly turned their attention to PS activation using carbon-based catalysts. Among them, biochar, a carbon-rich material produced from biomass pyrolysis, has gained attention as a sustainable and cost-effective catalyst for persulfate activation. Its unique properties, such as a high surface area, porous structure, abundant surface functional groups, and tunable electronic characteristics, make it highly effective for catalytic applications.[22] These features provide numerous active sites and mechanisms for persulfate activation, facilitating the generation of reactive species for pollutant degradation. The porous structure enhances pollutant and persulfate adsorption, while oxygen-containing groups and persistent free radicals play a key role in electron transfer during activation.[20,23] When modified to be magnetic, biochar can be more easily recovered and reused after water treatment, thereby improving its sustainability. Metal-loaded biochars can improve catalytic performance due to the combined effects of the biochar and the metal.[24] However, pristine biochar remains a more environmentally friendly option as it eliminates the risk of metal leaching, while still achieving adequate degradation, and avoids the complex modification processes involved in preparing metal-based biochars.

Previous research has reported the use of pristine biochar as an effective catalyst for activating PS to degrade organic pollutants in water.[5,25–31] However, stability, reusability, and the lack of a simple and effective regeneration process remain the main drawbacks of the unmodified biochar, which are important factors for practical application in the PDS activation. For example, Li *et al.*[30] utilized the biochar derived from sawdust and rice husk to activate PDS for the degradation of acid orange 7 (AO7). The efficiency of the catalyst drastically decreased by 40.2% for sawdust biochar and 71.5% for rice husk biochar in the 2nd run after 240 min. In another study, Lie *et al.*[27] observed similar stability issues with unmodified biochar (RBC800) in PMS-activated SMX degradation, with a 25.7% efficiency drop after four cycles. Reactivation required high-energy thermal treatment (450 °C, 2 h, N_2), yet only restored 74% efficiency, showcasing biochar's poor reusability and the impractical energy demands for large-scale AOP applications.

To address these challenges, this study focuses on the preparation of an efficient pristine biochar from pumpkin seed pomace, an agro-industrial byproduct rich in proteins, carbohydrates, minerals, and residual lipids and γ-tocopherol,[32] which yields heteroatom-doped carbon structures with embedded nitrogen and oxygen functionalities upon pyrolysis. These features collectively enable multiple active sites for both radical and non-radical persulfate activation pathways. Accordingly, the main objectives of this work are to: (i) synthesize pristine biochar from pumpkin seed pomace and evaluate its ability to activate PDS for RhB removal from water, (ii) comprehensively characterize the catalyst using multiple analytical techniques, (iii) assess the catalytic activity and mineralization efficiency of the biochars, (iv) investigate their stability and demonstrate a simple, rapid, and low-energy grinding-based regeneration method, and (v) identify the dominant reactive oxygen species, examine the influence of water matrix components, and propose a mechanistic pathway for PDS activation.

2. Materials and methods

2.1. Materials

The feedstock, Pumpkin seed pomace, was provided by the Vivi Oil Factory in Sulaymaniyah, Iraq. Rhodamine B (RhB, ≥99%)

was purchased from ACROS ORGANICS. Sodium persulfate (PDS, ≥99%), sodium hydroxide (NaOH, ≥99%), sodium chloride (NaCl, ≥99.5%), and nitrobenzene (NB, ≥99%) were purchased from Biochem Chemopharma. Ethanol absolute (EtOH), *p*-benzoquinone (*p*-BQ, ≥98%), sulfuric acid (H_2SO_4, 98%), and sodium carbonate anhydrous ($NaCO_3$, ≥99.5%) were purchased from Sigma-Aldrich. L-Histidine (L-H, ≥99%) was purchased from Riedel-de haen AG. Sodium nitrate ($NaNO_3$, ≥98%) was purchased from EMD Chemicals. Sodium phosphate ($NaH_2PO_4 \cdot 2H_2O$, ≥99%) from Alpha Chemika. All chemicals were used as received without further purification, and reagents were prepared using deionized water.

2.2. Preparation of biochars

The pristine biochars were synthesized by a facile and one-step pyrolysis. The waste of pumpkin seed pomace was ground, sieved (mesh-60), and then placed in an oven at 80 °C for 18 h to remove moisture. The dried material was pyrolyzed at 600 and 800 °C under nitrogen conditions and a heating rate of 10 °C min^{-1} for 2 hours. The products were then sieved (80-mesh) and labeled as PS600 and PS800, respectively.

2.3. Characterization of biochars

The surface morphology and elemental composition of the samples were examined using field emission scanning electron microscopy coupled with energy dispersive X-ray spectroscopy (FESEM-EDS, MIRA 3, TESCAN). X-ray diffraction (XRD) patterns were obtained with a Philips PW 1730 diffractometer, utilizing Cu Kα radiation (Kα = 0.154 nm). Fourier transform infrared (FTIR) spectra were recorded with a PerkinElmer Spectrum One spectrometer over a wavelength range of 400–4000 cm^{-1}. An automated gas sorption analyzer (Autosorb – iQ, Quantachrome) was employed to acquire N_2 adsorption–desorption isotherms and to determine the specific surface area (SSA) and pore size distribution using the Brunauer–Emmet–Teller (BET) model and Barrett–Joyner–Halenda (BJH) method. X-ray photoelectron spectroscopy (XPS) was conducted with a ThermoFisher Scientific K-Alpha+ spectrometer to analyze the surface electronic states and compositions.

2.4. Degradation experiments

The degradation experiments were conducted in a 125-mL beaker at a temperature of 23 ± 2 °C on the magnetic stirrer (300 rpm). To 50 mL of RhB (10, 20, 30, 40 mg L^{-1}), and a specific amount of catalyst (1, 1.5, 2, 2.5 g L^{-1}) was dispersed, then from a 1 M persulfate stock solution, a specific volume was injected to make (5, 8, 10, 15 mM) at the initial pH of 5.18 (unadjusted) and 3, 7, 9, and 11 adjusted using 0.1 M NaOH and 0.1 M H_2SO_4 solutions. At predetermined time intervals, 3 mL was withdrawn from the reaction solution and filtered through a 0.45 μm fiberglass syringe filter to read the remaining RhB concentration at 554 nm *via* a Shimadzu UV-1800 UV spectrophotometer. To determine stability and reusability, the catalyst was collected by filtration, dried in an oven at 60 °C for 10 h, ground, and used for the next cycle. For all parametric studies (catalyst dosage, PDS concentration, pH, and initial RhB concentration), only the variable of interest was adjusted, while all other conditions were kept constant to allow direct comparison.

2.5. Analytical methods

A TOC analyzer (TOC-VCPH Shimadzu) was used to determine the total organic carbon (TOC) during the removal of RhB to assess the mineralization efficiency of the reaction. The point of zero charge (pH_{PZC}) of the biochar was determined using the salt addition method.[33] A series of 0.01 M NaCl solutions was prepared, the pH of the solution was adjusted to (2, 4, 6, 8, 10, and 12) using 0.1 M solutions of H_2SO_4 and NaOH, and the pH values were assigned as pH_i. Subsequently, 0.1 g of biochar was added, and the mixture was stirred for 6 hours at 300 rpm and soaked for 18 h. After the supernatant had settled, the pH of each beaker was then measured, and the results were denoted by pH_f. The *x*-intercept of the ΔpH ($pH_f - pH_i$) plotted against pHi was used to calculate pH_{PZC}.

The total organic carbon (TOC) removal efficiency was determined *via* eqn (3) below.

$$\text{TOC removal efficiency } (\%) = \frac{TOC_0 - TOC_t}{TOC_0} \times 100 \quad (3)$$

where TOC_0 and TOC_t denote the TOC concentrations at initial ($t = 0$) and at time '*t*', respectively.

The pseudo-first-order rate constant, k_{obs}, was calculated using eqn (4).

$$\ln \frac{C_0}{C} = kt \quad (4)$$

where C_0 and C represent the RhB concentrations at the initial point and at time t, respectively; k signifies the observed pseudo-first-order reaction rate constant (min^{-1}); and t indicates the reaction duration (min).

The removal efficiency of the pollutant was calculated using eqn (5)

$$\text{Pollutant removal efficiency } (\%) = \frac{C_0 - C_t}{C_0} \times 100 \quad (5)$$

where C_0 and C_t are the concentrations of the pollutant at the initial time ($t = 0$) and reaction time (t), respectively.

3. Results and discussion

3.1. Biochar characterization

The BET-specific surface area (BET-SSA) and the BJH pore size distribution of the prepared catalysts were determined through nitrogen sorption isotherm measurements. The N_2 sorption isotherms (Fig. 1a) show distinctive features for each biochar sample. PS600 shows a Type I isotherm, which suggests it has a mostly microporous structure. This means it has a sharp increase in adsorption at low relative pressures, then levels off at higher pressures. On the other hand, the fresh PS800 sample has a Type I isotherm with a hysteresis loop. This indicates a more complicated pore structure, with both micropores and mesopores. The BET-SSA of PS600 and fresh PS800 were found to be 10.6 and 12.7 $m^2\ g^{-1}$, respectively. This difference is

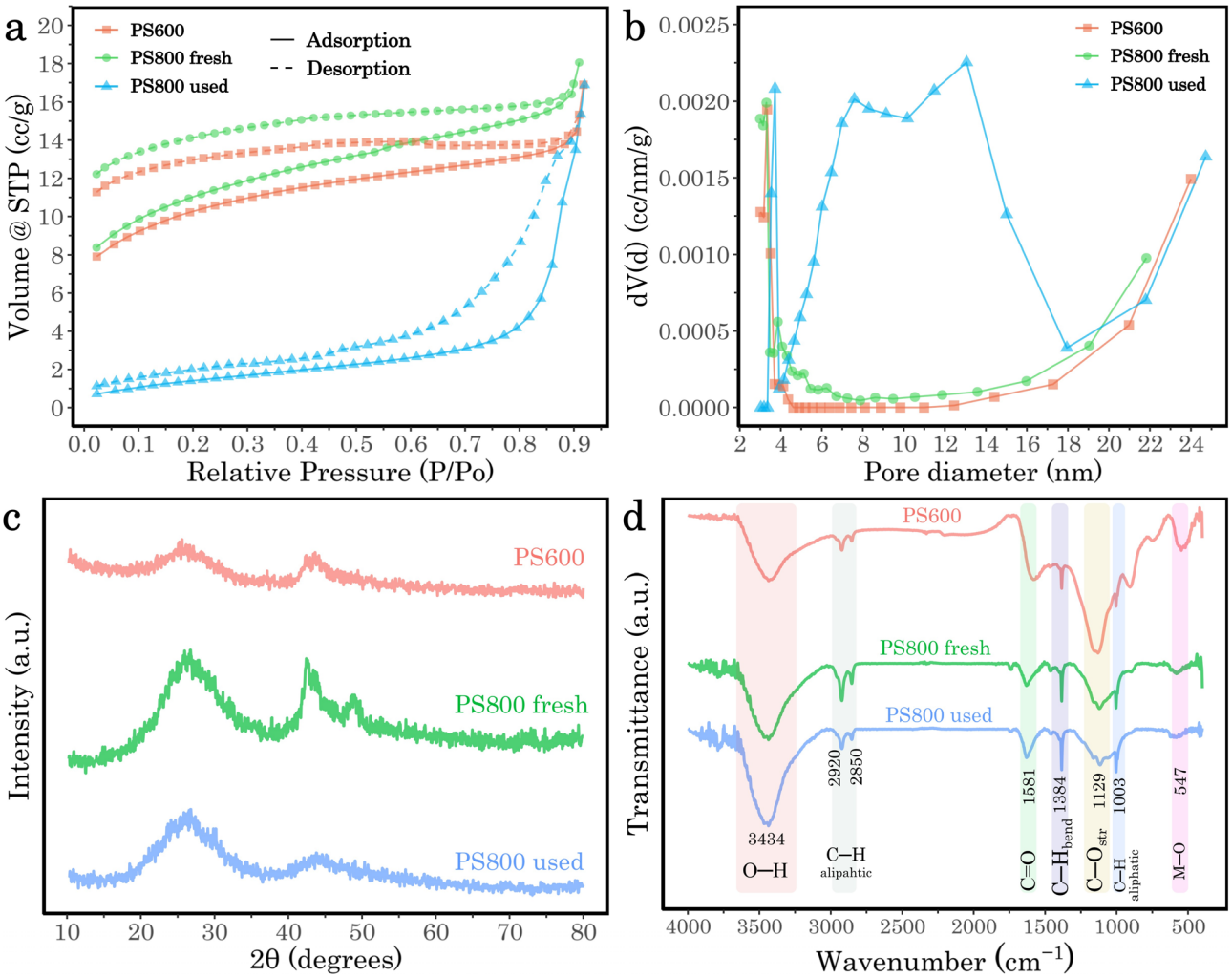

Fig. 1 (a) Nitrogen sorption isotherms, (b) pore size distribution, (c) XRD patterns, and (d) FTIR spectra of various biochar samples.

probably because the higher pyrolysis temperature helps create larger pores. Interestingly, a significant change can be seen in the used PS800 sample, displaying a Type II isotherm. This type is usually seen in non-porous or macroporous materials. This significant loss of microporosity and surface area (5.4 $m^2 g^{-1}$) is possibly due to pores getting blocked or destroyed during the persulfate-based AOP process for Rhodamine B breakdown.

The pore size distribution curves obtained by the BJH method of the three biochar samples (Fig. 1b) show differences in the porous structure. Analyzing the pore size distribution curves obtained by the BJH method for the three biochar samples reveals distinct differences in their porous structures. PS600 and fresh PS800 show similar overall patterns, with a prominent peak in the micropore region (~4 nm) and a gradual increase in pore volume for larger pores (>15 nm). The fresh PS800 exhibits a slightly higher volume of micropores and small mesopores (2–10 nm) compared to PS600, indicating that the higher pyrolysis temperature enhanced the development of smaller pores. In contrast, the used PS800 shows a dramatically different pore size distribution curve. It has lost most of its micropore and small mesopore volume, as evidenced by the absence of peaks below 5 nm. However, it displays a series of distinct peaks in the mesopore range (5–25 nm), suggesting the formation or exposure of new mesopores during the AOP process. This significant change in pore structure for used PS800 likely results from pore collapse, blockage of smaller pores, or the creation of new pores through the oxidative process.

The XRD patterns of PS600, fresh PS800, and used PS800 biochar samples reveal differences in crystallinity and structural ordering (Fig. 1c). All samples exhibit two broad diffraction peaks located at 24° and 43°, which are assigned to the (002) and (101) planes of turbostratic or disordered graphitic carbon. As the pyrolysis temperature rises from 600 °C to 800 °C, the peak intensities show a slight increase, indicating that elevated temperature enhances the crystallinity of the PS600 and PS800 materials.[28,34] The emerging peak at $2\theta \approx 48°$ in the fresh PS800 is likely from the mineral phases in the sample detected by EDS analysis.[35] However, after use in the persulfate-based AOP, the used PS800 sample showed a reduction in the intensity of these peaks, suggesting that the biochar's crystallinity has degraded, likely due to oxidative attack and amorphization during the Rhodamine B degradation process. This indicates that the

ordered structure of fresh PS800 becomes less pronounced after exposure to the PDS conditions, leading to a partially degraphitized or disordered carbon structure in used PS800.

In the FTIR spectra of PS600, fresh PS800, and used PS800 biochar samples, key peaks reveal the presence of various functional groups. As illustrated in Fig. 1d, for PS600, the broadband at 3434 cm^{-1} corresponds to O–H stretching vibrations from hydroxyl groups or adsorbed water, while peaks at 2920 and 2850 cm^{-1} are due to C–H stretching in aliphatic hydrocarbons or residual organic matter. The band at 1581 cm^{-1} indicates C=C stretching in aromatic rings, highlighting the presence of aromatic carbon structures. In the fresh PS800 sample, these peaks, especially the O–H stretching band, decrease in intensity, suggesting fewer hydrophilic groups due to higher pyrolysis temperatures, while the C=C band remains stable, reflecting the durability of aromatic structures. New peaks at 1384 cm^{-1} (C–H bending) and 1129 and 1003 cm^{-1} (C–O stretching in ethers, alcohols, or phenols) also appear. For the used PS800, most of the peaks were observed to be relatively unchanged except for the peak at 547 cm^{-1}, which likely indicates the reduction of metal oxide.

The EDS spectra and corresponding elemental weight percentages for PS600, fresh PS800, and used PS800 are presented in Fig. 2a. All three biochar samples are predominantly composed of carbon (C) and oxygen (O), which are characteristic of biomass-derived biochars. Significant amounts of nutrient elements such as phosphorus (P), nitrogen (N), potassium (K), and magnesium (Mg), along with trace amounts of calcium (Ca), iron (Fe), and copper (Cu), were also detected, originating from the pumpkin seed biomass. Comparing PS600 and Fresh PS800, increasing the pyrolysis temperature from 600 °C to 800 °C resulted in a slight decrease in nitrogen content (from 4.61% to 3.25%), likely due to volatilization at the higher temperature. Other elemental compositions remained relatively similar, with slight increases in oxygen and minor variations in P, K, and Mg. Analysis of the fresh PS800 *versus* the used PS800 revealed changes after the reaction with PDS for Rhodamine B degradation. Notably, the weight percentages of P and Mg increased on the used biochar surface (P: 4.47% to 6.27%; Mg: 1.98% to 3.10%). Conversely, there were decreases in the content of N, K, and Cu. The carbon and oxygen content remained largely stable. EDS analysis revealed that the wt% of K

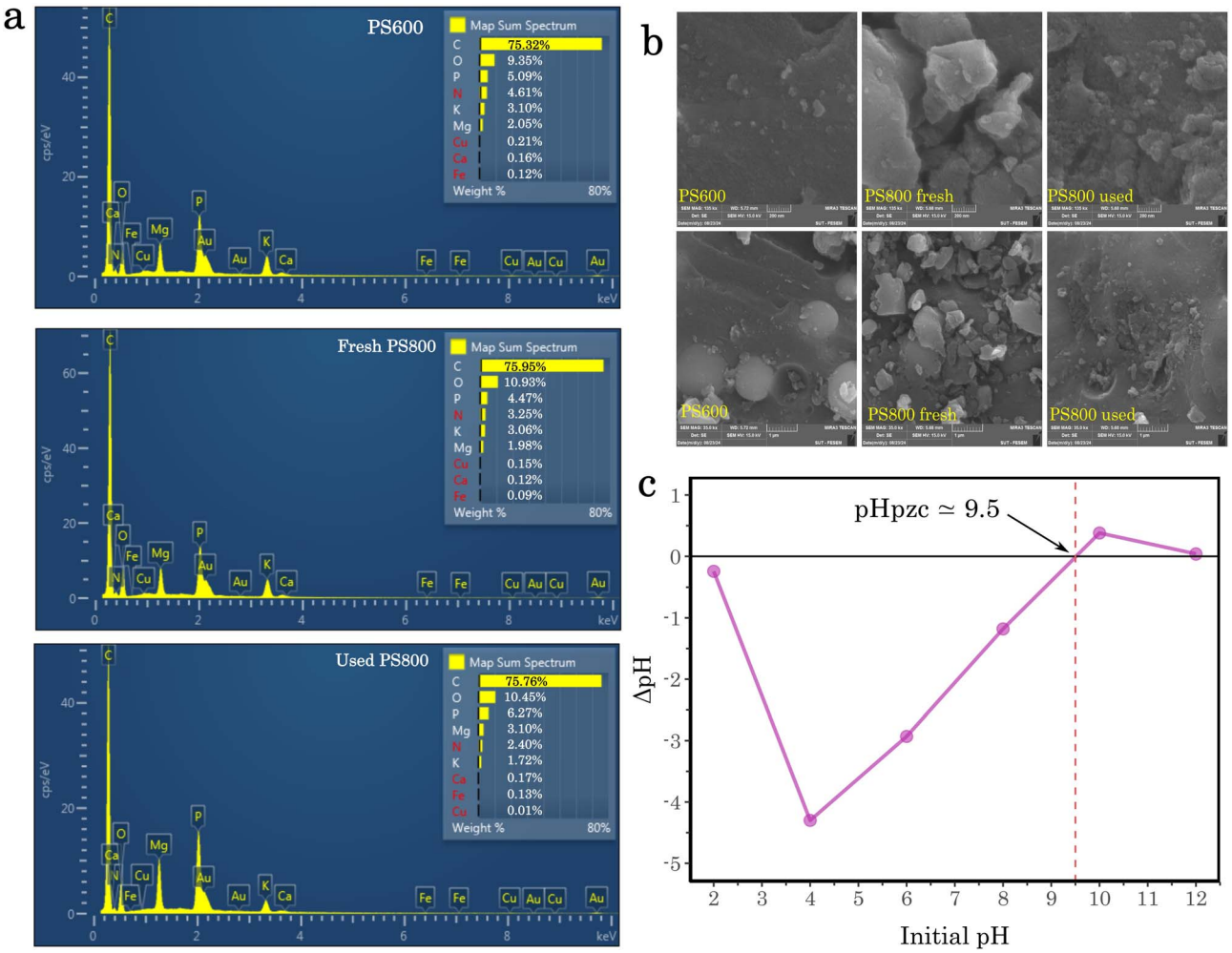

Fig. 2 (a) EDS spectra and weight percentage of each biochar. (b) SEM images of various biochars. (c) Determination of the point of zero charge (pH_{pzc}) of the PS800 biochar.

decreased from 3.06% to 1.72% and Cu from 0.15% to 0.01% in used PS800 compared to fresh PS800. This suggests that some mineral species were consumed or leached during persulfate activation. However, given their low abundance and the fact that they were not detected by XPS on the catalyst surface, their contribution to persulfate activation is considered insignificant. These changes suggest potential interactions between the biochar surface and components of the reaction medium during the catalytic process, possibly involving adsorption or leaching of certain species.

The SEM images (Fig. 2b) reveal distinct morphological differences among the three biochar samples, with PS800 exhibiting a more fragmented and irregular structure with visible interparticle spaces, consistent with the enhanced pore development observed in N_2 sorption analysis. The used PS800 shows a significant transformation in morphology, with a rougher surface texture and the presence of numerous small, granular particles deposited on the surface. This change likely results from the persulfate-based AOP treatment, which may have caused surface etching, deposition of reaction products, or the formation of new surface features. The altered surface of the used PS800 confirms the changes observed in its pore size distribution, indicating that the SR-AOP process not only affected the internal pore structure but also significantly modified the external surface morphology of the biochar.

The point of zero charge (pH_{pzc}) of the PS800 biochar sample was determined to be 9.5 (Fig. 2c), indicating that the surface charge of the biochar is pH dependent. Below pH 9.5, the biochar surface exhibits a positive charge, while above pH 9.5, the surface becomes negatively charged. This amphoteric nature of the biochar suggests the presence of both acidic and basic functional groups on its surface. The relatively high pH_{pzc} value of 9.5 indicates a high density of basic functional groups on the biochar surface.

X-ray Photoelectron Spectroscopy (XPS) was employed to further investigate the surface elemental composition and chemical states of the biochars. The survey spectra (Fig. 3a and the inset table) confirmed the presence of carbon, oxygen, and nitrogen as the primary surface elements for PS600, fresh PS800, and used PS800. Consistent with EDS and pyrolysis principles, PS800 exhibited a higher atomic percentage (at%) of C and lower N compared to PS600, attributed to increased carbonization and volatilization at the higher temperature. Comparing fresh and used PS800, a slight increase in surface C and N at% and a decrease in O at% were observed after the reaction, hinting at surface modifications during the catalytic process.

High-resolution C 1s spectra (Fig. 3b) for fresh and used PS800 were deconvoluted to identify different carbon bonding states. Both samples showed dominant peaks corresponding to sp^2 hybridized carbon (graphitic C) at 283.73 eV and sp^3 hybridized carbon at 284.53 eV, along with contributions from C–O (285.81 eV) and C═O (287.46 eV) functionalities.[36] After reaction (used PS800), there was a notable increase in the relative proportions of C–O (11.12% to 15.21%) and C═O groups (4.84% to 11.16%), accompanied by changes in the sp^2/sp^3 carbon ratio and a significant decrease in the π–π^* satellite feature. This suggests that the carbon structure underwent oxidation and modification during the catalytic activation of peroxydisulfate.

The O 1s spectra (Fig. 3c) revealed significant changes in oxygen-containing functional groups upon reaction. In fresh PS800, C–OH (51.99%) was the dominant species, followed by C═O (32.54%) and C–O (ether/epoxy, 15.48%). After use, the proportion of C–OH drastically decreased (to 7.43%), while C–O groups became the most abundant species (59.6%). The relative amount of C═O remained relatively stable. This dramatic shift strongly indicates the involvement of surface hydroxyl and ether/epoxy groups in the catalytic cycle.

Analysis of the high-resolution N 1s spectra (Fig. 3d) provided insights into the role of nitrogen species. Fresh PS800 contained pyridinic N (35.16%), pyrrolic N (54.94%), and graphitic N (9.9%). After the reaction, the proportion of pyridinic N decreased significantly (to 25.51%), while pyrrolic N increased (to 64.9%). Pyridinic N species are often considered active sites in carbon materials. The observed decrease suggests that pyridinic N sites on the PS800 surface likely participate actively in the PDS activation process for dye degradation.

3.2. Evaluation of catalytic activity and mineralization

The catalytic activity of the prepared catalysts was evaluated by the degradation of RhB as a model pollutant in the reaction condition of $[RhB]_0 = 20$ mg L^{-1}, catalyst = 2 g L^{-1}, [PDS] = 10 mM, pH = 5.18 (unadjusted), $T = 23 \pm 2$ °C. The adsorption results, as shown in Fig. 4a, indicated little removal of RhB by PS600 (0.53%) and PS800 (7.59%) alone, showing the weak adsorption capacity of the biochars. Degradation efficiency was greatly enhanced after the incorporation of biochar catalysts with PDS. The PS800/PDS system was more efficient, with an excellent RhB removal of 99.38%, and it also showed the highest pseudo-first-order rate constant $k = 0.1644$ min^{-1}, with the PS600/PDS system showing 91.16% removal in 30 min, $k = 0.0722$ min^{-1} (Fig. 4b). Both biochar-catalyzed systems were superior to the PDS-only system, which removed only 51.33% of RhB, with $k = 0.0236$ min^{-1}, thus indicating the catalytic effect of biochars. The reason for this increased performance of PS800 over PS600 is the higher pyrolysis temperature, which should ensure a more developed porous structure with a larger surface area and thus better activation of PDS and RhB degradation. The results indicate that both pumpkin seed pomace biochars could be used as effective and sustainable catalysts for SR-AOP, with a particular focus on PS800. Therefore, PS800 was chosen to evaluate other parameters (catalyst dose, PDS concentration, pH, and initial RhB concentration).

The optimization of catalyst dosage is important for developing cost-effective and efficient SR-AOP for pollutant removal. The effect of PS800 biochar dosage on SR-AOP for RhB degradation was investigated as depicted in Fig. 4c. It was shown that the catalyst dose and RhB removal effectiveness were directly correlated. At the lowest dose of 1 g L^{-1}, PS800 achieved a 93.83% RhB removal within 30 min, with a k of 0.0872 min^{-1}. The degrading performance was gradually improved by increasing the catalyst dose; at 1.5 g L^{-1} and 2 g L^{-1}, RhB

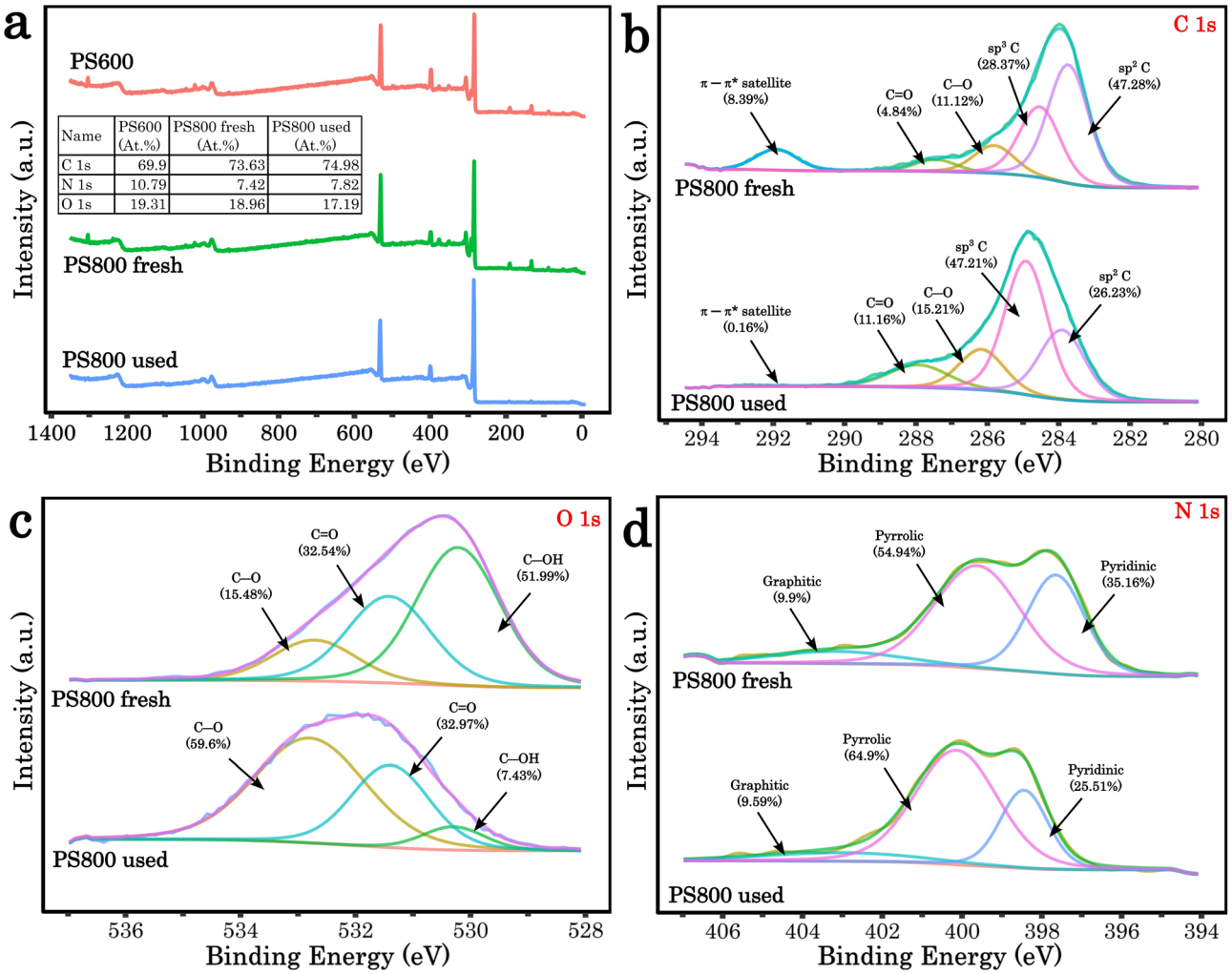

Name	PS600 (At.%)	PS800 fresh (At.%)	PS800 used (At.%)
C 1s	69.9	73.63	74.98
N 1s	10.79	7.42	7.82
O 1s	19.31	18.96	17.19

Fig. 3 XPS analysis. (a) Survey spectra of PS600 and fresh PS800 and used. (inset) Table of atomic percentages for C, O, and N. High-resolution spectra for fresh and used PS800: (b) C 1s, (c) O 1s, and (d) N 1s.

removal was 97.56% and 99.38%, respectively, with higher rate constants of 0.1220 min^{-1} and 0.1626 min^{-1}. The highest dose of 2.5 g L^{-1} had the best results, with 100% RhB removal in 30 min and having the highest rate constant of 0.2013 min^{-1}. This pattern can be explained by the fact that with greater catalyst dosages, there are more active sites available for PDS activation, which increases the production of sulfate radicals that aid in the breakdown of RhB.

The influence of PDS concentration is shown in Fig. 4d. The results showed that the PDS concentration and RhB removal efficiency were positively correlated. With the concentration of 5 mM PDS, 92.11% of RhB was removed in 30 minutes by the PS800/PDS system with a k of 0.0763 min^{-1}. The degradation performance was improved by increasing the PDS concentration: at 8 mM, 10 mM, and 15 mM, RhB was removed at rates of 98.66%, 99.38%, and 99.81%, respectively. These results were accompanied by higher rate constants of 0.1352 min^{-1}, 0.1626 min^{-1}, and 0.1875 min^{-1}. The observed trend can be attributed to the increased availability of sulfate radicals for RhB degradation with higher PDS concentration, as more PDS molecules are activated by the PS800 biochar to generate sulfate radicals.

As shown in Fig. 4e, the effect of pH on RhB degradation by the PS800/PDS system was examined over a range of starting pH values. The results showed that the PS800/PDS system performed well throughout a wide pH range (3–11), with over 99% RhB removal accomplished in 30 minutes for each condition. At pH 5.18 (near-neutral), the degradation efficiency reached its peak with 99.38% RhB removal and a k value of 0.1626 min^{-1}. Slightly lower but comparable performances were observed at pH 3 (99.14%, k = 0.1542 min^{-1}), pH 7 (99.14%, k = 0.1542 min^{-1}), pH 9 (99.28%, k = 0.1562 min^{-1}), and pH 11 (99.14%, k = 0.1547 min^{-1}). The PS800/PDS system appears to be largely pH-insensitive based on the small fluctuation in degradation efficiency and rate constants over the pH range. The observed pH-independence can be explained by the combined actions of many radical species and non-radical species ($^1O_2$) produced at varying pH levels, in addition to the possible buffering ability of the surface of the biochar.[19,37] The PS800/PDS system's ability to degrade RhB without the need for

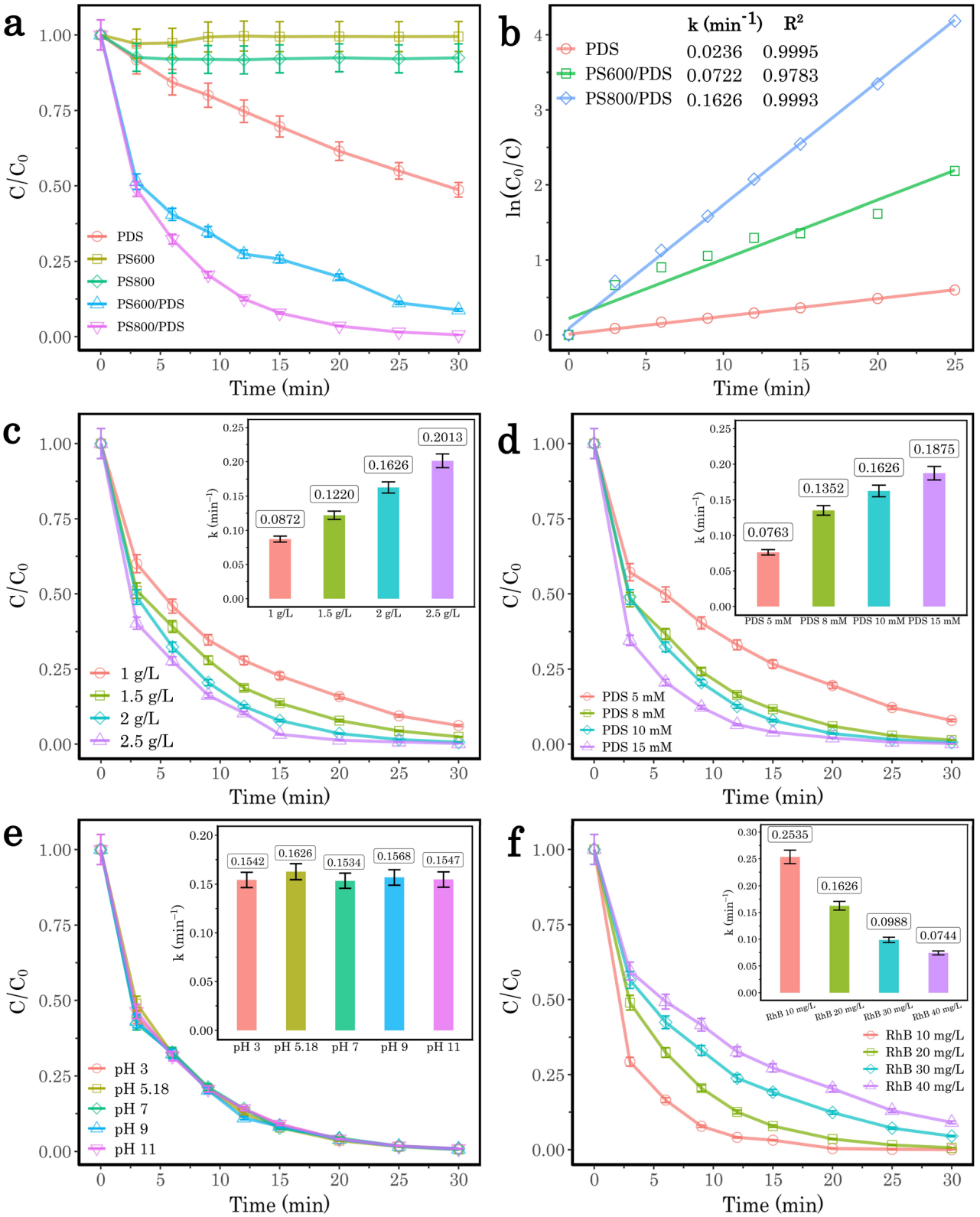

Fig. 4 (a) RhB removal performance under various systems, and the inset table is the TOC removal efficiency of the PS800/PDS system at the optimum condition. (b) Plot of $\ln(C_0/C)$ *versus* time, effect of (c) catalyst dose, (d) PDS concentration, (e) initial pH, and (f) initial RhB concentration; insets are the rate constant. Reaction condition: RhB = 20 mg L^{-1}, catalyst = 2 g L^{-1}, PDS = 10 mmol L^{-1}, initial pH = 5.18 (unadjusted), T = 23 ± 2 °C. In all experiments (panels a–f), only the parameter under investigation was varied, while all other reaction conditions were held constant.

stringent pH control or modification is demonstrated by its strong performance throughout a broad pH range, which is useful for practical wastewater treatment applications.

The influence of varying RhB concentrations on the performance of the PS800/PDS system in an SR-AOP was investigated. As illustrated in Fig. 4f, the results revealed an inverse relationship between initial RhB concentration and degradation efficiency. The system exhibited its peak performance at the lowest concentration of 10 mg L^{-1}, achieving a 99.62% removal rate in 20 min with a k of 0.2535 min^{-1}. As RhB concentration increased, a notable decline in both removal efficiency and rate constants was observed. The system's effectiveness diminished to 96.46% removal (k = 0.1626 min^{-1}) at 20 mg L^{-1}, further decreasing to 87.63% (k = 0.0988 min^{-1}) and 79.66% (k = 0.0744 min^{-1}) for 30 mg L^{-1} and 40 mg L^{-1}, respectively. This trend can be attributed to the fixed number of reactive species generated by the PS800/PDS system, which become overwhelmed at higher pollutant concentrations.

To determine the degree of mineralization of RhB in the PS800/PDS system at the optimum condition, the TOC of the solution was measured after 30 and 60 min. As shown in the inset of the Fig. 4a, the TOC removal efficiency was 53.7% and 81.4% in 30 and 60 min, respectively. These results indicate the effectiveness of the PS800/PDS system in the mineralization of RhB in aqueous media, which is an important factor in the degradation of organic pollutants.

3.3. Reusability and regeneration of the catalyst

The reusability of PS800 in the PDS system was evaluated over five cycles, as shown in Fig. 5a and b. Initially, Cycle 1 demonstrated high catalytic activity, achieving a 99.38% pollutant removal with a rate constant of 0.164 min^{-1}. However, a significant decline occurred in Cycle 2, where removal efficiency dropped to 83.83% (k = 0.061 min^{-1}), likely due to surface fouling or pore blockage by degradation by-products, as confirmed by SEM and BET, reducing active site accessibility. However, regenerating the catalyst through grinding, named Cycle R2, restored its activity to 99.03% removal (k = 0.150 min^{-1}), highlighting the importance of physical structure for catalytic function. Subsequent cycles (3–5), which included pre-use grinding, demonstrated consistent performance with only minor efficiency reductions: 98.40% (Cycle R3), 98.36% (Cycle R4), and 96.63% (Cycle R5), with k values declining from 0.138 to 0.113 min^{-1}. This regeneration strategy contrasts sharply with previous reports. For example, Zhu *et al.*[29] required thermal treatment at 300 °C for 2 h in air, Liu *et al.*[27] employed 450 °C under N_2, and Karim & Aziz[5] regenerated almond pomace biochar by re-pyrolysis at 600 °C. These methods, while partially effective, involve substantial energy input and specialized equipment. In comparison, our grinding method restored >99% removal efficiency in the third cycle and maintained >96% after five cycles, with negligible energy and cost requirements. This suggests that physical regeneration *via* grinding effectively mitigates major deactivation, while the minor efficiency losses in later cycles could stem from trace chemical degradation or minor structural wear rather than irreversible damage. Overall, the catalyst demonstrates strong reusability, with grinding as a simple and fast, yet effective regeneration strategy.

3.4. ROS identification

The role of reactive oxygen species (ROS) in the persulfate (PDS) system activated by the PS800 catalyst was investigated through quenching experiments using specific scavengers (Fig. 5c and d). The addition of scavengers revealed distinct contributions of different ROS. Ethanol (EtOH), which quenches both sulfate radicals ($SO_4^{\cdot-}$) and hydroxyl radical ($^{\cdot}OH$), ($k_{EtOH+{}^{\cdot}OH}$ = 1.2–2.8 × 10^9 M^{-1} s^{-1}; $k_{EtOH+SO_4^{\cdot-}}$ = 1.6–7.7 × 10^7 M^{-1} s^{-1}),[38] caused a sharp decline to 73.80% removal (k = 0.0513 min^{-1}), suggesting these radicals collectively contribute to degradation. Nitrobenzene (NB), which selectively scavenge $^{\cdot}OH$ compared to $SO_4^{\cdot-}$ ($k_{NB+{}^{\cdot}OH}$ = 3.9 × 10^9 M^{-1} s^{-1}; $k_{NB+SO_4^{\cdot-}} \leq 4 \times 10^6$ M^{-1} s^{-1}),[39] reduced removal efficiency from 98.48% (k = 0.1626 min^{-1}) to 88.80% (k = 0.0752 min^{-1}), indicating partial reliance on $^{\cdot}OH$. The most pronounced inhibition occurred with L-histidine (L-H), a singlet oxygen ($^1O_2$) scavenger ($k_{^1O_2+L\text{-}H}$ = 3.0 × 10^7 M^{-1} s^{-1}),[38] which drastically lowered removal to 36.57% (k = 0.0158 min^{-1}). This highlights $^1O_2$ as the dominant ROS driving the process. In contrast, *p*-benzoquinone (*p*-BQ), a superoxide radical ($O_2^{\cdot-}$) scavenger ($k_{O_2^{\cdot-}+BQ}$ = 9.6 × 10^8 M^{-1} s^{-1}),[38] showed moderate suppression (70.94% removal, k = 0.047 min^{-1}), implying a secondary role for $O_2^{\cdot-}$. These results demonstrate that $^1O_2$ is the primary oxidative species in the PS800/PDS system, with sulfate and hydroxyl radicals playing supplementary roles. The minimal activity in the presence of L-H shows the system's heavy dependence on singlet oxygen. The non-radical mechanism can also explain the pH independence of the PS800/PDS system.[40]

3.5. Effect of water matrices

Natural water contains inorganic anions and natural organic matter (NOM), which may influence the degradation of organic pollutants. Consequently, for practical applications, the impact of these matrix components must be systematically evaluated. To address this, the effect of water matrix components on RhB degradation in the PS800/PDS system was assessed by individually introducing various anions and humic acid (HA) into the reaction, as illustrated in Fig. 5e and f. The addition of CO_3^{2-} resulted in a significant reduction in both k (0.047 min^{-1}) and removal efficiency (75.86%), indicating strong inhibition. This pronounced effect may be attributed to carbonate ions reacting with the $O_2^{\cdot-}$ which is essential for producing $^1O_2$, slowing the reaction kinetics.[41] In contrast, NO_3^- and Cl^- exhibited minimal interference, with removal efficiencies of 98.29% and 98.91%, and k of 0.128 and 0.146 min^{-1}, respectively, comparable to the control (98.38% and 0.163 min^{-1}). These results suggest that nitrate and chloride ions do not appreciably interact with the PS800 surface, preserving the system's reactivity. Moderate inhibition was observed with $H_2PO_4^-$ and HCO_3^-, which yielded removal efficiencies of 96.48% and 94.01%, respectively, alongside reduced k values (0.106 and 0.085 min^{-1}). These anions may interact with the catalyst

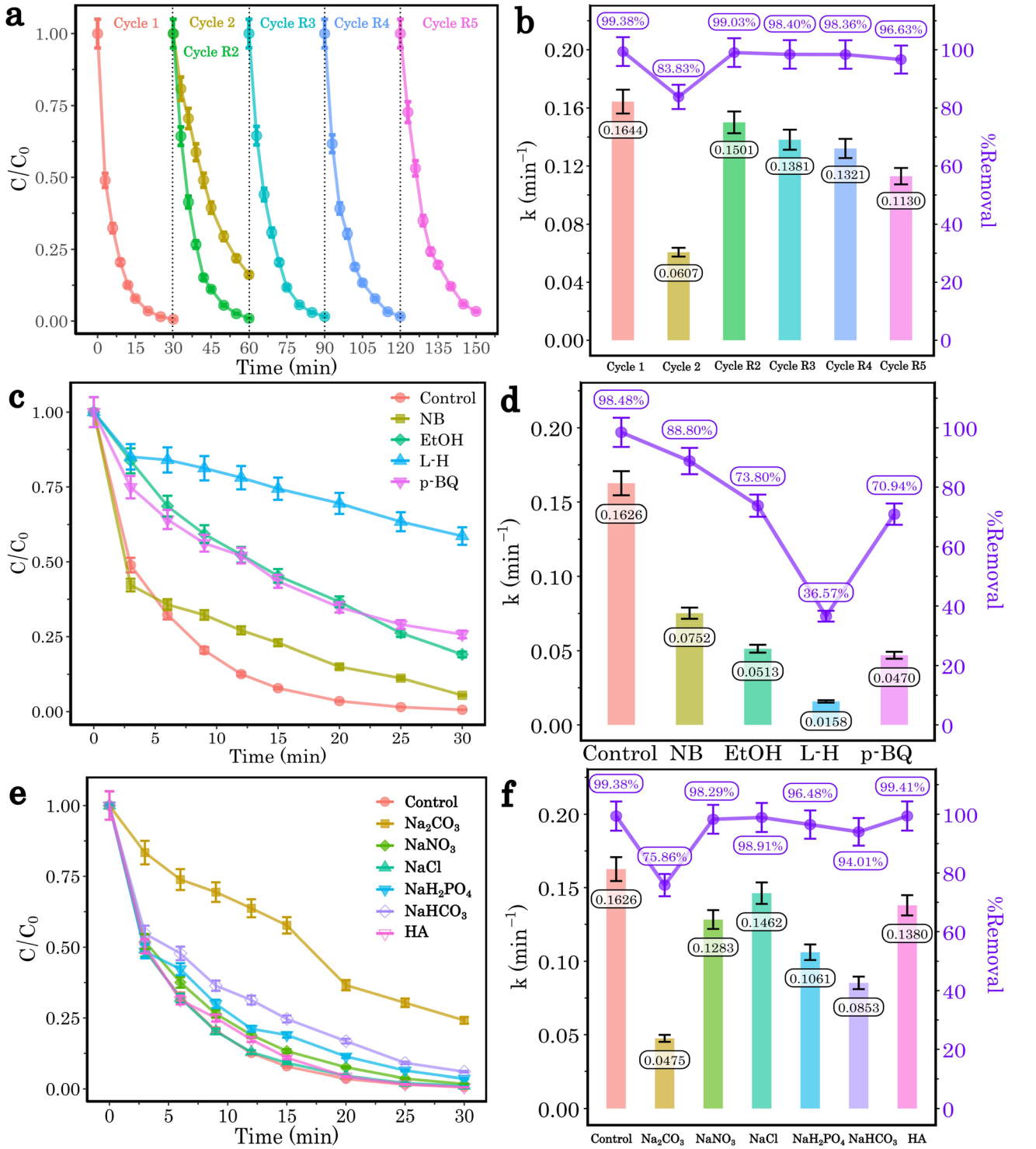

Fig. 5 (a) Reusability test of PS800 for five cycles, (b) rate constant and removal efficiency for the five cycles. (c) Quenching tests using various scavengers, and (d) their corresponding rate constant and removal efficiency; concentration of scavengers: [EtOH] = 5000 mmol L^{-1}, NB = 100 mg L^{-1}, *p*-BQ = 20 mM, L-H = 20 mM. (e) Effects of water matrices, and (f) their corresponding rate constant and removal efficiency; concentration of anions and humic acid: [Na_2CO_3] = [$NaNO_3$] = [NaCl] = [NaH_2PO_4] = [$NaHCO_3$] = 10 mmol L^{-1}, [HA] = 50 mg L^{-1}. Reaction condition: RhB = 20 mg L^{-1}, catalyst = 2 g L^{-1}, PDS = 10 mmol L^{-1}, initial pH = 5.18 (unadjusted), $T = 23 \pm 2$ °C.

surface, though their effects were less severe than CO_3^{2-}. Similarly, HA showed negligible impact, achieving 99.41% removal with a k of 0.138 min^{-1}, nearly matching the control, highlighting the resilience of the system to HA, a common component of natural organic matter. This is most likely due to the non-radical generation mechanism of the PS800/PDS

system. Overall, the PS800/PDS system demonstrated robustness against common anions like nitrate, chloride, and HA, but sensitivity to carbonate highlights the need for careful matrix consideration in practical applications.

3.6. Proposed mechanism of ROS generation

Based on XPS analysis, reusability tests, and ROS quenching results, a mechanism for ROS generation in the PS800/PDS system is proposed (Fig. 6). According to the XPS deconvoluted O 1s (Fig. 3c), the proportion of C–OH drastically decreased from 52% to 7.43%. This indicates the activation of $S_2O_8^{2-}$ ions adsorbed on the catalyst surface by the C–OH groups to generate $SO_4^{-\bullet}$ (eqn (6)).[29] The $^{\bullet}OH$ can form from the reaction of $SO_4^{-\bullet}$ and H_2O/OH^-, as shown in eqn (7). Compared to fresh PS800, the used PS800 exhibited a significant decrease in π–π* content, falling from 8.39% to 0.16% (Fig. 3b). This reduction suggests that π–π* transitions were consumed during the oxidation reaction. Similarly, sp^2 content declined from 47.28% to 26.23%. These observations indicate that the π–π* transitions in the graphitic structure of PS800 also serve as active sites for decomposing surface-bound $S_2O_8^{2-}$ complex and generating $SO_4^{-\bullet}$ and SO_4^{2-} (eqn (8)).[25,27] According to the quenching study, $^1O_2$ was the main ROS responsible for the RhB degradation (Fig. 5c and d). Pyridinic N sites on the PS800 surface are likely involved in the activation of PDS, as its proportion decreased from 35.16% to 25.51% in XPS deconvoluted N 1s (Fig. 3d). PDS readily binds to the catalyst surface, creating a carbon-$S_2O_8^{2-}$ complex. Following this, the pyridinic N functions as Lewis basic sites, donating electrons to the electrophilic oxygen of the carbon-$S_2O_8^{2-}$ complex.[42] This electron transfer then triggers the cleavage of the O–O bond, yielding HO_2^- and SO_4^{2-} (eqn (9)).[43] The HO_2^- can then react with the $S_2O_8^{2-}$ to produce $O_2^{-\bullet}$ and $SO_4^{-\bullet}$ (eqn (10)). Also, the dissolved oxygen can accept an electron from the biochar active site to form $O_2^{\bullet-}$ (eqn (11)).[44] The $O_2^{-\bullet}$ generated undergoes protonation to form hydroperoxyl radical ($HO_2^{\bullet}$) in aqueous media (eqn (12)).[45] Subsequently, $^1O_2$ forms *via* two disproportionation pathways: the self-reaction of $HO_2^{\bullet}$ radicals (eqn (13)) and the cross-disproportionation between $HO_2^{\bullet}$ and $O_2^{-\bullet}$ (eqn (14)).[42,46,47] Residual minerals like potassium and copper can activate PDS by donating electrons to generate $=SO_4^{-\bullet}$, as shown in eqn (15). This is supported by their decreased weight percentages in EDS and the loss of the XRD peak at $2\theta \approx 48°$ after the reaction. However, their contribution to PDS activation is negligible due to their low concentration in the biochar and undetectable XPS signals on the catalyst surface. The generated ROS, primarily $^1O_2$, attack and degrade the RhB molecules adsorbed on the biochar surface or present in the bulk solution to smaller molecules or mineralize to H_2O and CO_2 (eqn (16)). Overall, the catalyst's surface facilitates the adsorption of both PDS and RhB molecules. Subsequently, its hydroxyl groups, pyridinic N, and graphitic structure act as active sites, enabling PDS activation and RhB degradation, with the mineral species playing a minor role.

$$BC_{surf.}\text{–}OH + S_2O_8^{2-} \rightarrow SO_4^{-\bullet} + HSO_4^- + BC_{surf.}\text{–}O^{\bullet} \quad (6)$$

$$SO_4^{-\bullet} + H_2O \rightarrow OH^{\bullet} + SO_4^{2-} + H^+ \quad (7)$$

$$\pi\text{-electrons} + S_2O_8^{2-} \rightarrow SO_4^{-\bullet} + SO_4^{2-} \quad (8)$$

$$S_2O_8^{2-} + 2H_2O \rightarrow HO_2^- + 2SO_4^{2-} + 3H^+ \quad (9)$$

$$S_2O_8^{2-} + HO_2^- \rightarrow SO_4^{-\bullet} + SO_4^{2-} + H^+ + O_2^{\bullet-} \quad (10)$$

$$BC + O_2 \rightarrow BC^+ + O_2^{-\bullet} \quad (11)$$

$$O_2^{\bullet-} + H_2O \rightarrow HO_2^{\bullet} + OH^- \quad (12)$$

$$HO_2^{\bullet} + HO_2^{\bullet} \rightarrow {}^1O_2 + H_2O_2 \quad (13)$$

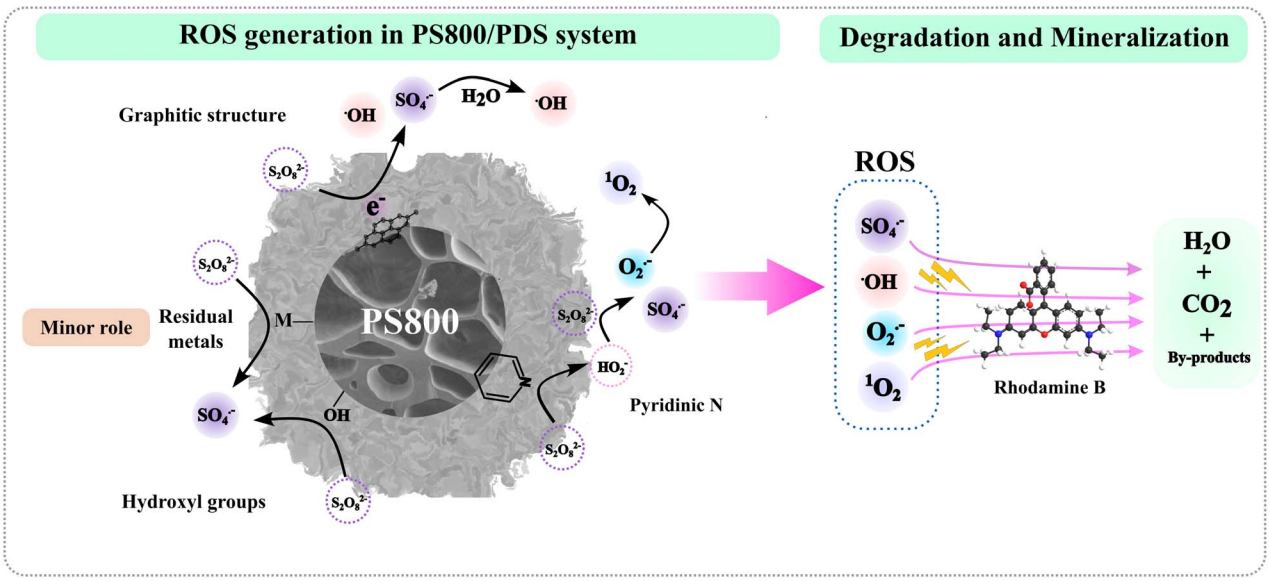

Fig. 6 Proposed mechanism for ROS generation in the PS800/PDS system.

Table 1 Comparative analysis of pristine biochar catalysts in persulfate-based AOPs

Feedstock	Pollutant	Removal efficiency (per cycle)	Reaction conditions	Regeneration method	Ref.
Sawdust	Acid orange 7	1st: >90%	Catalyst: 1.5 g L^{-1}; persulfate: 9 mmol L^{-1}; pH: 6	Oven drying at 80 °C for 12 hours	28
Wood (poplar sawdust)	Acid orange 7	1st: 99.6%; 2nd: 87.5%; 3rd: 58.9%; 4th: 39%	Catalyst: 0.5 g L^{-1}; persulfate: 10 mM; pH: 6.0	Thermal treatment at 300 °C for 2 hours in air	29
Sawdust and rice husk	Acid orange 7	Sawdust (1st): ∼100%; (2nd): ∼60% Rice husk (1st): ∼100%; (2nd): ∼28.5%	Catalyst: 1.0 g L^{-1}; persulfate: 40 : 1 (PS/AO7 molar ratio); pH: not specified (natural)	Not specified. Reuse without regeneration	30
Corn stalk	Norfloxacin	1st: 94.21%; 2nd: 70.22%; 3rd: 40.84%	Catalyst: 0.8 g L^{-1}; persulfate: 120 : 1 (PS/NOR molar ratio); pH: 6.5	Not specified. Reuse without regeneration	26
Wood (poplar)	Clofibric acid	1st: 97.8%; 2nd: ∼93.7%; 3rd: ∼90.1%; 4th: ∼56.9%	Catalyst: 0.5 g L^{-1}; persulfate: 10 mM; pH: 4.0	Thermal treatment at 300 °C for 2 hours in air	25
Rice husk	Sulfamethoxazole	1st: 92.0%; 2nd: ∼80%; 3rd: ∼74%; 4th: ∼66.3%	Catalyst: 0.4 g L^{-1}; peroxymonosulfate: 0.6 mM; pH: 7.0	Thermal treatment at 450 °C for 2 hours under N_2 flow	27
Almond pomace	Rhodamine B	1st: 99.98%; 2nd: 62.84%; 3rd (regenerated): 99.79%; 4th: 94.4%; 5th: 86.83%	Catalyst: 1.5 g L^{-1}; persulfate: 10 mM; pH: 5.3	Pyrolysis at 600 °C for 1 hour	5
Pine needles	Enrofloxacin	1st: 97.7% (within 180 min); 3rd: 30.7%; after re-pyrolysis at 700 °C for 1 h: 56.8%	ENR: 50 mg L^{-1}; PMS: 0.3 mM; biochar (BC-700): 30 mg; pH ≈ 7; 25 °C; 180 min reaction	Re-pyrolysis at 700 °C for 1 h partially restores activity	31
Pumpkin seed pomace	Rhodamine B	1st: 99.38%; 2nd: 83.83%; 3rd (regenerated): 99.03%; 4th: 98.36%; 5th: 96.63%	Catalyst: 2 g L^{-1}; persulfate: 10 mM; pH: 5.18	Simple grinding	This study

$$HO_2^{\cdot} + O_2^{\cdot -} \rightarrow {}^1O_2 + HO_2^- \quad (14)$$

$$BC\text{–}M^n + S_2O_8^{2-} \rightarrow SO_4^{-\cdot} + SO_4^{2-} + BC\text{–}M^{n+} \quad (15)$$

$$SO_4^{-\cdot}/OH^{\cdot}/{}^1O_2/O_2^{-\cdot} + RhB \rightarrow CO_2 + H_2O + \text{by products} \quad (16)$$

3.7. Comparative analysis with previous studies

While high initial removal efficiencies are common across different feedstocks, most studies report rapid deactivation after the first cycle or require energy-intensive regeneration methods such as thermal treatment at 300–700 °C or re-pyrolysis. These approaches, although partially effective, involve substantial energy input, specialized equipment, and high operational costs, limiting their scalability. In contrast, the present study demonstrates that PS800 can be effectively regenerated by a simple grinding method. This approach restored >99% removal efficiency in the third cycle and maintained >96% efficiency after five cycles, with negligible energy and cost requirements. The simplicity, economic feasibility, and sustained performance of this regeneration strategy represent a significant advancement in the practical application of pristine biochar for water remediation. Table 1 compares the performance and regeneration strategies of pristine biochar catalysts reported in persulfate-based AOPs.

4. Conclusions

This study demonstrated the synthesis of pristine biochar from waste pumpkin seed pomace and its highly efficient application in activating persulfate for RhB degradation. The PS800 biochar, pyrolyzed at 800 °C, exhibited superior structural properties and catalytic activity, achieving over 99% RhB removal and 81.4% TOC mineralization under optimized conditions. A key finding was the excellent stability and reusability of PS800 (96.63% efficiency after 5 cycles), particularly when a simple grinding regeneration step was employed, which effectively restored catalytic performance after deactivation. Additionally, this study demonstrated the environmental safety of the PS800, with no metal leaching, and its broad pH applicability in the PDS system. Mechanistic studies revealed that singlet oxygen was the primary reactive oxygen species responsible for RhB degradation, complemented by sulfate and hydroxyl radicals, with catalyst surface functionalities like C–OH groups, pyridinic N, and graphitic π–π* transitions playing crucial roles in PDS activation. The system's efficacy across a broad pH range and resilience to several common water matrix ions further highlight its practical potential. Therefore, pumpkin seed pomace biochar presents a promising, sustainable, and cost-effective alternative catalyst for persulfate-based advanced oxidation processes in water decontamination.

Conflicts of interest

There are no conflicts of interest to declare.

Data availability

All experimental data and analyses produced in this study are fully reported in the manuscript.

Acknowledgements

The authors thank the University of Sulaimani, Kurdistan-Iraq, for supporting the work and the Vivi oil factory for providing the pumpkin seed pomace.

References

1 T. Lewis Yusuf, B. O. Orimolade, D. Masekela, B. Mamba and N. Mabuba, *RSC Adv.*, 2022, **12**, 26176–26191.
2 V. Yalasangi, N. Mayilswamy and B. Kandasubramanian, *Bioresour. Technol. Rep.*, 2024, **28**, 101987.
3 A. Lesniewicz and A. Lewandowska-Andralojc, *Sci. Rep.*, 2024, **14**, 22600.
4 F. Verdini, D. Crudo, V. Bosco, A. V. Kamler, G. Cravotto and E. Calcio Gaudino, *Processes*, 2024, **12**, 2128.
5 M. A. H. Karim and K. H. Hama Aziz, *J. Water Process Eng.*, 2025, **75**, 108014.
6 J. Sharma, S. Sharma, U. Bhatt and V. Soni, *J. Hazard. Mater. Lett.*, 2022, **3**, 100069.
7 S. Samsami, M. Mohamadizaniani, M.-H. Sarrafzadeh, E. R. Rene and M. Firoozbahr, *Process Saf. Environ. Prot.*, 2020, **143**, 138–163.
8 S. Dutta, B. Gupta, S. Kumar Srivastava and A. Kumar Gupta, *Mater. Adv.*, 2021, **2**, 4497–4531.
9 B. M. Adesanmi, Y.-T. Hung, H. H. Paul, C. R. Huhnke, B. M. Adesanmi, Y.-T. Hung, H. H. Paul and C. R. Huhnke, *GSC Adv. Res. Rev.*, 2022, **10**, 126–137.
10 M. Tripathi, S. Singh, S. Pathak, J. Kasaudhan, A. Mishra, S. Bala, D. Garg, R. Singh, P. Singh, P. K. Singh, A. K. Shukla and N. Pathak, *Toxics*, 2023, **11**, 940.
11 R. Al-Tohamy, S. S. Ali, F. Li, K. M. Okasha, Y. A.-G. Mahmoud, T. Elsamahy, H. Jiao, Y. Fu and J. Sun, *Ecotoxicol. Environ. Saf.*, 2022, **231**, 113160.
12 V. Vinayagam, K. N. Palani, S. Ganesh, S. Rajesh, V. V. Akula, R. Avoodaiappan, O. S. Kushwaha and A. Pugazhendhi, *Environ. Res.*, 2024, **240**, 117500.
13 K. H. Hama Aziz, F. S. Mustafa, K. M. Omer and I. Shafiq, *Water Resour. Ind.*, 2023, **30**, 100227.
14 Z. Honarmandrad, X. Sun, Z. Wang, M. Naushad and G. Boczkaj, *Water Resour. Ind.*, 2023, **29**, 100194.
15 K. H. Hama Aziz, F. S. Mustafa, M. A. H. Karim and S. Hama, *Mater. Adv.*, 2025, **6**(11), 3433–3454.
16 S. Giannakis, K.-Y. A. Lin and F. Ghanbari, *Chem. Eng. J.*, 2021, **406**, 127083.
17 J. Wang and J. Tang, *Chemosphere*, 2021, **276**, 130177.
18 J. Lee, U. von Gunten and J.-H. Kim, *Environ. Sci. Technol.*, 2020, **54**, 3064–3081.
19 Z. Liu, C. Tan, Y. Zhao, C. Song, J. Lai and M. Song, *Chem. Eng. J.*, 2024, **485**, 149724.
20 S. M. Badiger and P. V. Nidheesh, *Water Sci. Technol.*, 2023, **87**, 1329–1348.

21 T. Zhou, C. Shi, Y. Wang, X. Wang, Z. Lei, X. Liu, J. Wu, F. Luo and L. Wang, *Water Sci. Technol.*, 2024, **90**, 824–843.
22 C. Zhao, B. Shao, M. Yan, Z. Liu, Q. Liang, Q. He, T. Wu, Y. Liu, Y. Pan, J. Huang, J. Wang, J. Liang and L. Tang, *Chem. Eng. J.*, 2021, **416**, 128829.
23 Y. Zhang, M. Xu, S. Liang, Z. Feng and J. Zhao, *Sci. Total Environ.*, 2021, **794**, 148707.
24 F. S. Mustafa and K. H. Hama Aziz, *Process Saf. Environ. Prot.*, 2023, **170**, 436–448.
25 K. Zhu, X. Wang, M. Geng, D. Chen, H. Lin and H. Zhang, *Chem. Eng. J.*, 2019, **374**, 1253–1263.
26 B. Wang, Y. Li and L. Wang, *Chemosphere*, 2019, **237**, 124454.
27 T. Liu, C.-X. Li, X. Chen, Y. Chen, K. Cui and Q. Wei, *Int. J. Mol. Sci.*, 2024, **25**, 11582.
28 J. He, Y. Xiao, J. Tang, H. Chen and H. Sun, *Sci. Total Environ.*, 2019, **690**, 768–777.
29 K. Zhu, X. Wang, D. Chen, W. Ren, H. Lin and H. Zhang, *Chemosphere*, 2019, **231**, 32–40.
30 F. Li, F. Duan, W. Ji and X. Gui, *Ecotoxicol. Environ. Saf.*, 2020, **198**, 110653.
31 S. Pei, Y. Zhao, W. Li, C. Qu, Y. Ren, Y. Yang, J. Liu and C. Wu, *Chem. Eng. J.*, 2023, **477**, 147274.
32 N. Polyzos, Â. Fernandes, R. C. Calhelha, J. Petrović, M. Soković, I. C. F. R. Ferreira, L. Barros and S. A. Petropoulos, *Plants*, 2024, **13**, 2395.
33 H. N. Tran, S.-J. You and H.-P. Chao, *Waste Manag. Res.*, 2016, **34**, 129–138.
34 Y. Hu, D. Chen, R. Zhang, Y. Ding, Z. Ren, M. Fu, X. Cao and G. Zeng, *J. Hazard. Mater.*, 2021, **419**, 126495.
35 H. Huang, J. Tang, K. Gao, R. He, H. Zhao and D. Werner, *RSC Adv.*, 2017, **7**, 14640–14648.
36 X. Chen, X. Wang, D. Fang and F. Nanotub, *Carbon Nanostruct.*, 2020, **28**, 1048–1058.
37 H. Xie, X. Zhang, X. Jia, D. Xu, Z. Wu, F. Li, W. Yao and Y. Zhang, *Sep. Purif. Technol.*, 2025, **354**, 129237.
38 G. Manickavasagam, C. He, K.-Y. A. Lin, M. Saaid and W.-D. Oh, *Environ. Res.*, 2024, **252**, 118919.
39 J. R. J. Zaeni, J.-W. Lim, Z. Wang, D. Ding, Y.-S. Chua, S.-L. Ng and W.-D. Oh, *Sep. Purif. Technol.*, 2020, **241**, 116702.
40 J. Yu, L. Tang, Y. Pang, X. Liang, Y. Lu, H. Feng, J. Wang, L. Deng, J. Zou, X. Zhu and J. Tang, *Chem. Eng. J.*, 2022, **433**, 134385.
41 S. Zhang, J. Xu, Y. Zhong, X. Liang and S. Wang, *Mater. Today Commun.*, 2024, **39**, 108694.
42 S. Qu, Y. Yuan, X. Yang, H. Xu, A. K. Mohamed, J. Zhang, C. Zhao, L. Liu, B. Wang, X. Wang, J. Rinklebe, Y. C. Li and S. Wang, *Chem. Eng. J.*, 2022, **441**, 135864.
43 C. Wang, R. Huang, R. Sun, J. Yang and M. Sillanpää, *J. Environ. Chem. Eng.*, 2021, **9**, 106267.
44 J. Liu, Z. Yao, G. Qiu, Y. Wan, W. Song, H. Zeng, F. Yang, D. Zhao, W. Yuan, P. Ju, R. Lin, H. Zhou, L. Shi and K. Hu, *Chem. Eng. J.*, 2023, **455**, 140602.
45 J. Qu, J. Wang, Y. Xu, Y. Hu, S. Yan, W. Tong, G. Zhang, Q. Hu and Y. Zhang, *Colloids Surf., A*, 2025, **726**, 137845.
46 D. Guo, S. You, F. Li and Y. Liu, *Chin. Chem. Lett.*, 2022, **33**, 1–10.
47 Z. Pi, X. Li, D. Wang, Q. Xu, Z. Tao, X. Huang, F. Yao, Y. Wu, L. He and Q. Yang, *J. Cleaner Prod.*, 2019, **235**, 1103–1115.